ACCSCIENCE PUBLISHING

International Journal of Bioprinting

RESEARCH ARTICLE

A mobile drop-on-demand laser-assisted printing head integrated with a robotic arm and a target tracking system

Ahad Mohammadi[1,2], Shakiba Davani[1,2], and Christos Boutopoulos[1,2,3]*

[1]Institute of Biomedical Engineering, University of Montreal, Montreal, Quebec, Canada

[2]Centre de Recherche Hôpital Maisonneuve-Rosemont, Montreal, Quebec, Canada

[3]Department of Ophthalmology, University of Montreal, Montreal, Quebec, Canada

Abstract

In this work, we present a mobile drop-on-demand (DoD) printing system based on laser-induced side transfer (LIST). By replacing the bulky free-space optics used in previous LIST configurations with a fiber-based laser delivery system, we developed a compact printing head and integrated it as an end-effector onto a robotic arm. Using model inks with viscosities up to 165 cP and time-resolved imaging, we investigated printability, printing dynamics, and the effect of printing head-to-substrate distance on key printing quality metrics. We found that printing quality deteriorates significantly beyond a 3 mm standoff distance. To address motion-induced printing quality loss on dynamic substrates, we integrated a custom-built fiber-optic distance sensor that actively maintains a constant standoff distance in real time. This enabled high-quality printing on moving targets simulating physiological motion. Additionally, we characterized the influence of ink viscosity and laser energy on droplet formation dynamics and ejected volume. Our results demonstrate the feasibility of motion-compensated, laser-assisted DoD printing in dynamic environments, with potential applications in intraoperative tissue engineering.

Keywords: Drop-on-demand; Distance sensor; *In situ* bioprinting; Laser-induced side transfer; Motion compensation; Robotic

***Corresponding author:**
Christos Boutopoulos (christos.boutopoulos@umontreal.ca)

Citation: Mohammadi A, Davani S, Boutopoulos S. A mobile drop-on-demand laser-assisted printing head integrated with a robotic arm and a target tracking system. *Int J Bioprint*. doi: 10.36922/IJB025320321

Received: August 8, 2025
Revised: September 13, 2025
Accepted: September 16, 2025
Published online: September 17, 2025

1. Introduction

Bioprinting involves the deposition of cells and biomaterials to create functional tissues and organ models.[1] It emerged from the broader field of additive manufacturing, which gained momentum in the 1980s. Over time, various bioprinting technologies—such as inkjet, extrusion, and light-based printing—have been developed to address specific needs in printing resolution, speed, and cell viability.[2] Compared to traditional 2D cell cultures, bioprinting enables the fabrication of 3D tissue models that offer more physiologically relevant data for drug testing[3] and may help reduce the reliance on animal experimentation.[4,5] Additionally, bioprinting holds significant promise for advancing regenerative medicine by enabling the creation of patient-specific tissue constructs and reducing dependence on conventional transplantation methods.[6]

Bioprinting is increasingly focused on directly depositing bioinks onto patient tissues, enabling rapid, on-site clinical interventions.[7–10] To support these *in situ* applications, portable and versatile bioprinting systems are needed to navigate the human body—something conventional, bulky benchtop bioprinters cannot achieve. Notably, laser-based bioprinters[11,12] reported for *in situ* applications have been limited to stationary systems without maneuverability. Conversely, handheld bioprinters and robotic arms equipped with extrusion-based depositors have been used to attain the maneuverability required for more complex *in situ* printing applications.[9,13,14]

Achieving reliable *in situ* bioprinting requires the printing head to adapt to physiological movements, as the body may still move under anesthesia due to breathing or involuntary motions.[15] This is critical for maintaining printing resolution and preventing tissue injury. Early *in situ* tissue engineering efforts struggled to maintain print fidelity under dynamic conditions, resulting in low-quality constructs.[16,17] However, with advances in sensor technologies and robotic control, motion compensation has been explored as a solution. By integrating real-time motion compensation, bioprinters can eventually adapt to patient movements, ensuring consistent high-quality prints. Recent studies demonstrate that robotic systems with image-based motion compensation can be used to counteract simulated physiological movements.[14,18]

Among bioprinting techniques, drop-on-demand (DoD) methods—such as inkjet printing,[19] laser-induced forward transfer (LIFT),[20–24] and laser-induced flow focusing[25]—are particularly well suited for applications requiring non-contact biomaterial deposition. Recently, our laboratory introduced a DoD method termed laser-induced side transfer (LIST)[26] for printing low- to moderate-viscosity bioinks. LIST has been successfully tested for printing primary cells, including human umbilical vein endothelial cells and sensory neurons, while maintaining high post-printing viability.[26,27] The latest version of LIST employs continuous bioink perfusion through a glass capillary with a laser-machined hole serving as a nozzle and utilizes focused, low-energy nanosecond laser pulses for droplet ejection.[28] However, all previous implementations of LIST have relied on a bulky free-space beam delivery system, preventing the mobility of the printing head.

Here, we introduced and validated a mobile printing head based on the LIST technique. Central to our approach is the replacement of a bulky free-space beam delivery system with a fiber-based alternative. The mobile printing system was mounted on a robotic arm, and a model ink (with viscosity up to 165 cP), along with a time-resolved imaging setup, was used to study printability and printing dynamics. We investigated how variations in the distance between the printing head and the target substrate affect printing quality. Finally, we developed and validated an automated distance-tracking system based on a fiber-optic sensor to compensate for printing quality degradation when printing on moving substrates that mimic physiological motion in patients.

2. Materials and methods

2.1. Model ink

A water–glycerol mixture was used as a model ink with different mixing ratios, producing a viscosity range from 2.8 to 165 cP.[29] We used a single viscosity (18 cP) to test printability on moving substrates, while the full viscosity range was applied in the second part of the study to investigate the effects of viscosity on bubble formation, jetting dynamics, and printing volume. Due to the transparency of water in the visible range,[30] a biocompatible food dye, Allura Red AC (10 mM) (458848 100G, Sigma-Aldrich), was added to the ink to increase its absorption coefficient at 532 nm.

2.2. Microjet and bubble imaging

We used a time-resolved imaging approach to capture bubble and jet dynamics. The imaging system comprises a high-speed camera (Chronos 1.4; Kron Technologies, Canada), an achromatic lens (AC254-150-A-ML, Thorlabs, USA), an objective lens (RMS4X, Thorlabs), and an LED light source (MCWHL5; Thorlabs). A delay generator (DG535, Stanford Research Systems, USA) and a photodiode (DET10A, Thorlabs) were used to trigger image capturing at the desired time delays with respect to laser firing.

Microscopy images of printed drops were processed using a custom MATLAB script to quantify droplet placement error. The droplet placement error was calculated as the distance between the intended and actual drop landing positions. Droplet circularity, splatter coverage, and area were calculated using ImageJ (NIH, USA) and its built-in image processing tools. Splatter coverage was defined as the ratio of the total satellite drop area to the total main drop area.

2.3. Mobile LIST printing head

The core printing component of the mobile printing head is a glass microcapillary (8250; Vitrocom, USA; inner dimensions: 500 × 500 μm^2; wall thickness: 100 μm) continuously perfused with ink.[28] The capillary features a femtosecond laser-machined 200 μm circular opening on one of its sides, acting as a nozzle.[28] Laser pulses from a pulsed 532 nm Nd:YAG laser (Nano S 60-30; Litron Lasers, UK; 6 ns pulse duration) are used to generate microjets. Unlike our previous work that employed an open beam delivery system,[28] the laser used in this study was coupled

to a 105 μm core optical fiber (FG105LCA; Thorlabs), with the fiber fixed to the glass capillary opposite the laser-machined opening using a 3D-printed holder. This 3D-printed holder also incorporates clamps for the interchange of capillaries and tubing guides, securing both the tubing and fiber, with the entire assembly comprising the mobile printing head. A detailed 3D CAD rendering of the print head can be found in Figure S1, Supplementary File. A syringe pump (NE 1000; New Era Pump Systems Inc., USA) and perfusion tubing (89404-042; VWR, Canada) were used to continuously perfuse ink through the microcapillary at flow rates between 4 and 12 μL/min. The ink does not leak from the nozzle due to surface tension, and microjets are only generated when the delivered laser pulse induces bubble formation and a pressure increase inside the capillary.

2.3. Robotic arm integration and OCT-based distance tracking system

The mobile LIST printing head was mounted on a 5-axis robotic arm (Dorna 2, Dorna Robotics, USA). To simulate the physiological movement of the chest during breathing,[31] microscope slides used as printing substrates were displaced in the Z-axis with a 12 mm amplitude (24 mm peak-to-peak displacement) and a frequency of 0.2 Hz using a translation stage (Z825B, Thorlabs). The printing speed was 5 Hz, and the printing pattern consisted of an array of drops spaced 1.5 mm apart. The pattern was printed in a sequential row-wise pattern, starting with a horizontal line of droplets, followed by a vertical offset to print the next row below, and continuing in this alternating sequence. The z-position of the robotic arm was continuously updated using a distance tracking system to maintain the printing head at a fixed distance from the moving substrate. The distance tracking system automation is based on a homemade spectral-domain common-path optical coherence tomography (OCT) system that has been described in detail elsewhere.[32] For this work, a miniaturized (125 μm in thickness) fiber-based probe was attached to the printing head, emitting light toward the moving substrate. The backscattered light was collected by the same fiber probe and directed to the readout system. A single-mode fiber (SM800-5.6-125, Thorlabs) was used for the probe. To optimize light emission and collection, we spliced a 272-μm GRIN fiber (GIF625, Thorlabs) to the distal end of the single-mode fiber, resulting in a non-diverging light beam emission.[33] The axial resolution of the system was experimentally measured to be 18 μm.

A Python-based algorithm was used to control the entire automation, including processing the tracking system readout and controlling the robotic arm. The entire motion-tracking automation system operated at a frequency of 5 Hz. Real-time Z-axis correction required stepwise movement execution, with all coordinates updated at each step. The X and Y coordinates were predefined to follow the sequential row-wise scanning pattern described above, while the Z coordinate was dynamically calculated. Specifically, at each step, the Z-axis control logic compared the actual printing distance to the target distance (3 mm). If the deviation was less than 50 μm, the Z position remained unchanged; if the deviation exceeded 50 μm, the Z position was adjusted to offset the difference. While the fiber-based sensor operated at 50 Hz, the Python-based control script queried the sensor at 200-ms intervals (5 Hz). This update frequency was chosen as a compromise between minimizing vibrations in the robotic arm and ensuring sufficient sampling to track the substrate movement.

At a fixed standoff distance of 3 mm, droplet arrays were printed at both 2 and 5 Hz to investigate the effect of robotic arm vibrations on printing quality.

2.4. Statistical analysis

All reported values in this work represent the mean and standard deviation from three independent printing experiments. Data in Figure 3 were analyzed by one-way analysis of variance (ANOVA) using Prism 10 software (GraphPad Software, USA).

3. Results

3.1. Mobile LIST implementation

We implemented our mobile LIST printer using a modified version of our latest LIST configuration, which employs continuous ink perfusion through a square glass capillary (500 μm × 500 μm) with a 200 μm circular opening.[28] Our key modification involves replacing the free-space optics with a fiber delivery system (Figure 1), as detailed in the Section 2. The working principle of the printer remains identical to previous LIST implementations,[26–28,34,35] where the interaction of a pulsed laser (pulse duration: 6 ns, wavelength: 532 nm) with the ink within the glass capillary generates an expanding bubble that propels a microjet from the capillary opening (Figure 1A). The microjet eventually detaches from the opening, resulting in the deposition of a nanodroplet onto a receiving substrate. The fiber, connecting tubing, and glass capillary were assembled using a 3D-printed holder. The resulting mobile printing head was attached to a robotic arm as an end-effector (Figure 1B).

3.2. Influence of printing head-to-target distance on printing quality

The printing head-to-target distance is known to affect printing quality in DoD printing systems.[36] Quantifying

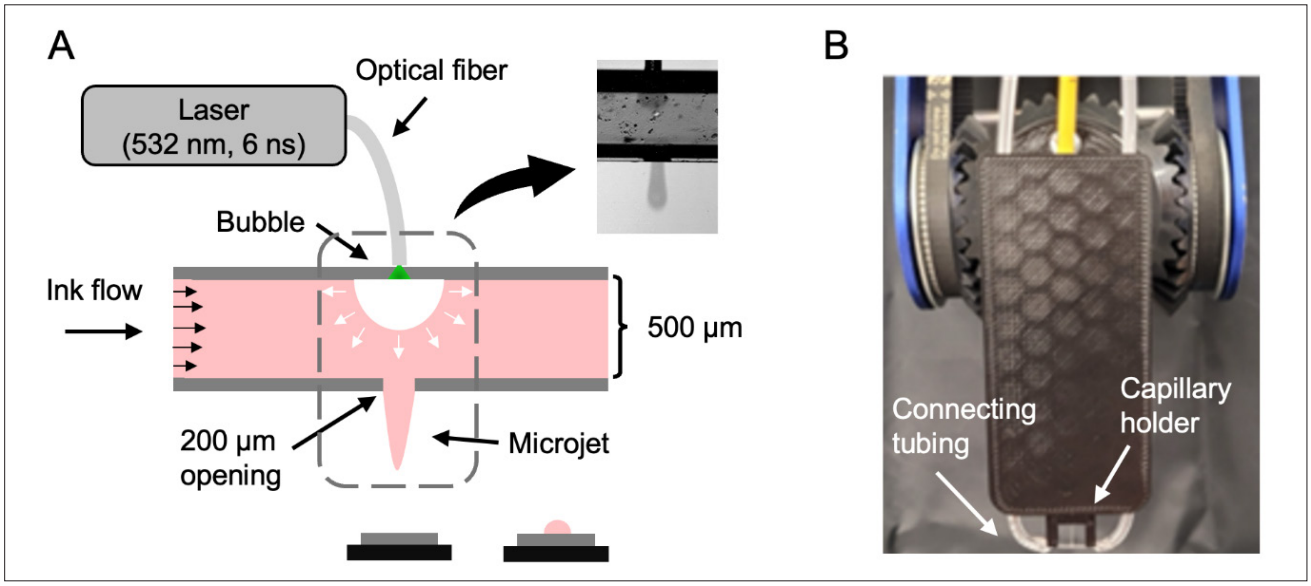

Figure 1. Fiber-based implementation of laser-induced side transfer (LIST) enables a mobile printing head and robotic integration. (A) Schematic overview of the mobile LIST printing head implementation. The inset is a high-speed camera image showing a bubble at the upper part of the capillary, below the fiber–capillary contact point, and a microjet exiting the fiber opening. (B) Photograph of the mobile LIST printing head mounted on a robotic arm as an end-effector.

this effect is important for identifying the operational window in *in situ* printing applications, including the maximum distance limit to maintain a desired level of printing quality. To address this for the mobile LIST printing head, we conducted printing experiments using a model ink (viscosity: 18 cP), varying the distance between the printing head and the target substrate (Figure 2A). Splatter coverage was used as the primary metric to quantify print quality.

Figure 2B shows optical microscopy images of arrays of model ink droplets printed at constant energy per pulse (230 µJ, corresponding to 1.15 times the printing threshold energy) across different printing head-to-target distances. The maximum range at which splatter coverage remained zero was 3 mm. Beyond this point, splatter coverage progressively increased, from 5.11 ± 2.03% at 6 mm to 37.36 ± 13.01% at 24 mm (Figure 2C). Secondary metrics of printing quality, such as drop placement error, drop circularity, and main drop area, followed the same trend. Drop placement error increased from 181 ± 94 µm at 1.5 mm to 383 ± 227 µm at 24 mm (Figure 2D). Drop circularity declined from 0.85 ± 0.12 to 0.69 ± 0.18 (Figure 2E), while the main drop area decreased from 1.29 ± 0.25 to 1.08 ± 0.31 mm^2 (Figure 2F), primarily due to the formation of satellite droplets.

Taken together, these printing quality metrics demonstrate that print quality degrades as the printing head-to-target distance increases. A distance of 3 mm is identified as a practical upper limit, where printing remains splatter-free.

3.3. Preventing printing quality loss in dynamic environments using a distance sensor

For dynamic printing environments where the printing target cannot be fixed (e.g., printing on living animals), the distance between the printing head and the target must be dynamically adjusted to maintain printing quality. We developed an optical fiber-based distance sensor using the OCT principle and integrated it with the mobile printing head and robotic arm to mitigate quality loss when printing on a moving substrate. The working principle of this automation is outlined in Figure 3A and detailed in Section 2.

We employed a dynamic z-position adjustment approach to print our model ink (viscosity: 18 cP) on a moving target that oscillated with a displacement amplitude of 12 mm (24 mm peak-to-peak displacement), representing the average chest expansion due to breathing.[31] Figure 3B shows optical microscopy images of arrays of model ink droplets printed at a constant energy per pulse (230 µJ, corresponding to 1.15-times the printing threshold energy) under three conditions: (i) a constant 3 mm printing head-to-target distance, (ii) target movement without compensation, and (iii) dynamic compensation, where the target moves while the printing head actively maintains a 3 mm distance.

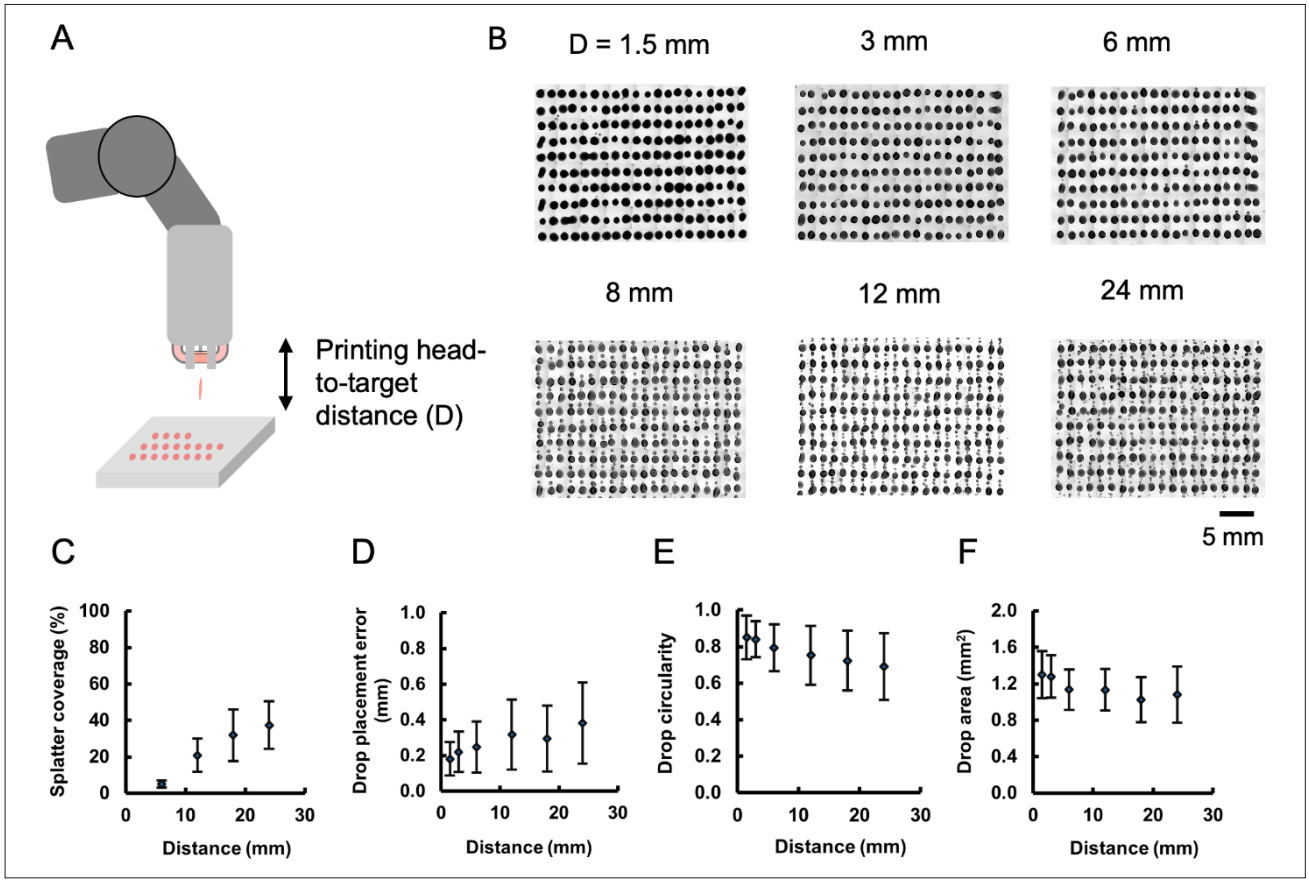

Figure 2. The impact of printing head-to-target distance on print quality. (A) Schematic overview of the approach used to investigate the effect of varying the printing head-to-target distance on print quality. (B) Optical microscope images of model ink arrays printed at different printing head-to-target distance. The effect of varying the printing head-to-target distance on (C) splatter coverage, (D) drop placement error, (E) drop circularity, and (F) drop area. Error bars represent the standard deviation from three independent printing experiments.

Figure 3C–F presents a quantitative analysis of the printing quality metrics under the three conditions. We found that printing on a moving target significantly worsened most printing quality metrics. Splatter coverage increased from 0.00 ± 0.00% to 34.17 ± 5.03% (p = 0.0003), drop circularity decreased from 0.84 ± 0.02 to 0.72 ± 0.05 (p = 0.0016), and the main drop area was reduced from 1.23 ± 0.05 to 1.09 ± 0.10 mm² (p = 0.0360). A similar trend was observed for the drop placement error, which increased from 220 ± 100 to 340 ± 80 μm (p = 0.0576). With dynamic compensation, all printing quality metrics improved, showing no statistically significant difference from printing on a stationary target (Figure 3C–F).

Taken together, these results demonstrate that the fiber-based LIST not only results in a small-footprint mobile system but also enables automation for printing in dynamic environments—something that was impossible with the initial LIST implementation,[28,34,35] which was based on free-space optics and a stationary printing head.

3.4. The effect of the ink viscosity and printing energy on the bubble and jetting dynamics

In DoD printing, the viscosity of the ink plays a crucial role in determining the efficiency and quality of the printing process.[37,38] Here we sought to understand its effect on the bubble and microjet dynamics using the mobile LIST printing head.

Figure 4A shows a microjet ejection from the printing head, with an indicative sequence of images captured using a high-speed camera. A bubble forms below the fiber tip, expands toward the opening, reaches its maximum size, and then collapses. Simultaneously, a microjet forms at the capillary opening, grows, and eventually detaches. Using multiple image sequences, we monitored bubble and jetting dynamics for a range of ink viscosity (2.8–165 cP). We found that the jet generation threshold increased with viscosity, ranging from 180 μJ for 2.8 cP to 260 μJ for

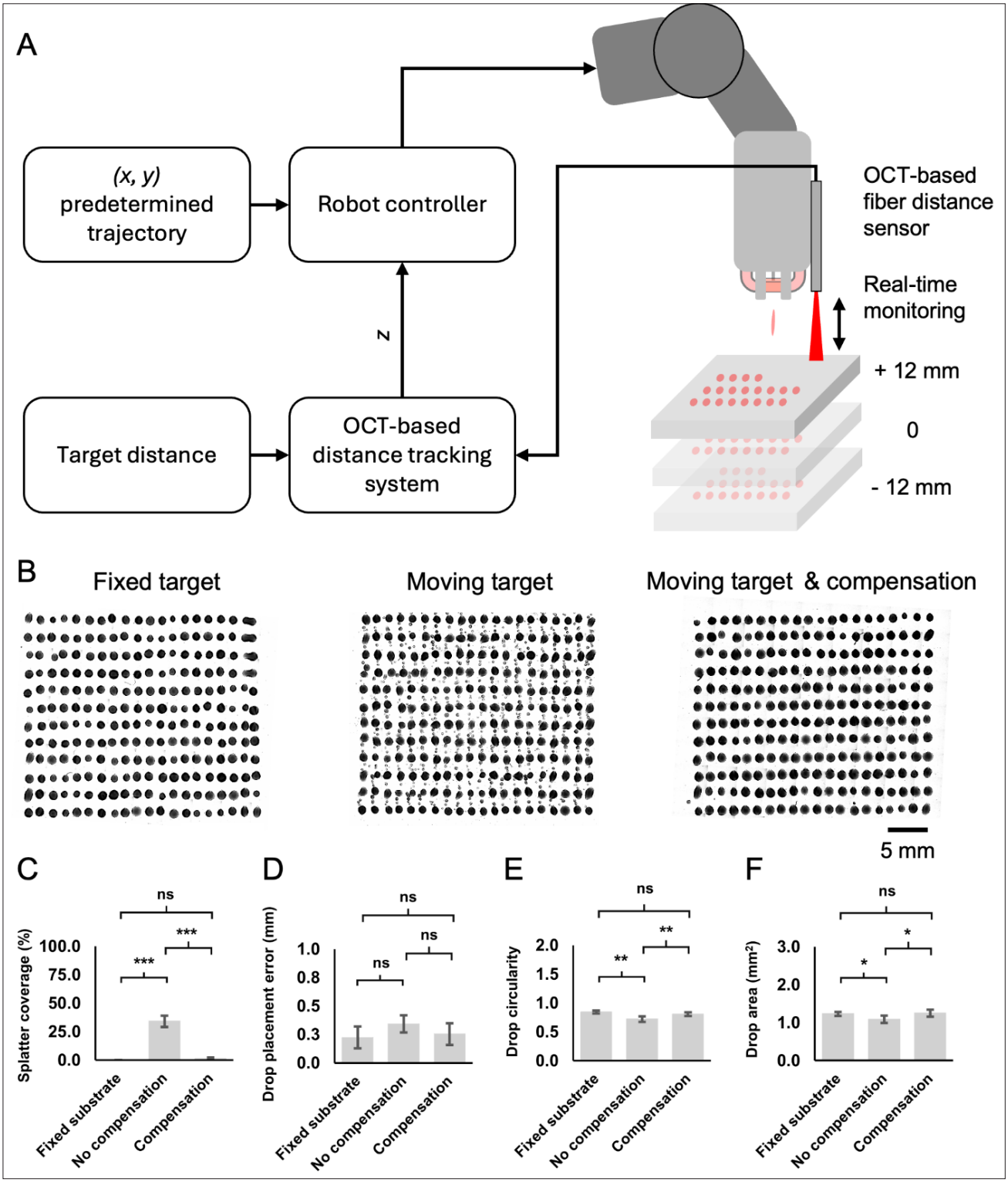

Figure 3. Positioning tracking ensures uncompromised printing quality on a moving target. (A) Flow chart of robot control for printing on a movable target using an optical coherence tomography (OCT) fiber-based distance tracking system. (B) Optical microscope images of model ink arrays printed using: a fixed 3 mm printing head-to-target distance (left), a moving target with a 12 mm amplitude (middle), a moving target with a 12 mm amplitude and dynamic z-position adjustment (right). The effect of the printing mode on: (C) splatter coverage, (D) drop placement error, (E) drop circularity, and (F) drop area at different printing head-to-target distances. Data in graphs (C) to (F) were analyzed using one-way ANOVA. Error bars represent the standard deviation from three independent printing experiments.

165 cP. The jet front position for three selected viscosities (2.8, 75, and 165 cP) is plotted up to the pinch-off time in Figure 4B, while the corresponding plots for all tested viscosities can be found in Figure S2, Supplementary File. Processing the linear part of the jet front allowed for the calculation of jet-ejection velocities for the examined conditions (Figure 4C). The jet velocity increased with the energy for all viscosities, covering the range of 0.78 ± 0.96 to 15.23 ± 0.90 m/s. The corresponding dynamic pressure ($P = \rho v^2/2$) varied from 0.34 ± 0.83 to 127 ± 15.08 kPa (Figure 4D). The jet velocity decreased with increasing viscosity for a given energy. Pinch-off times were observed

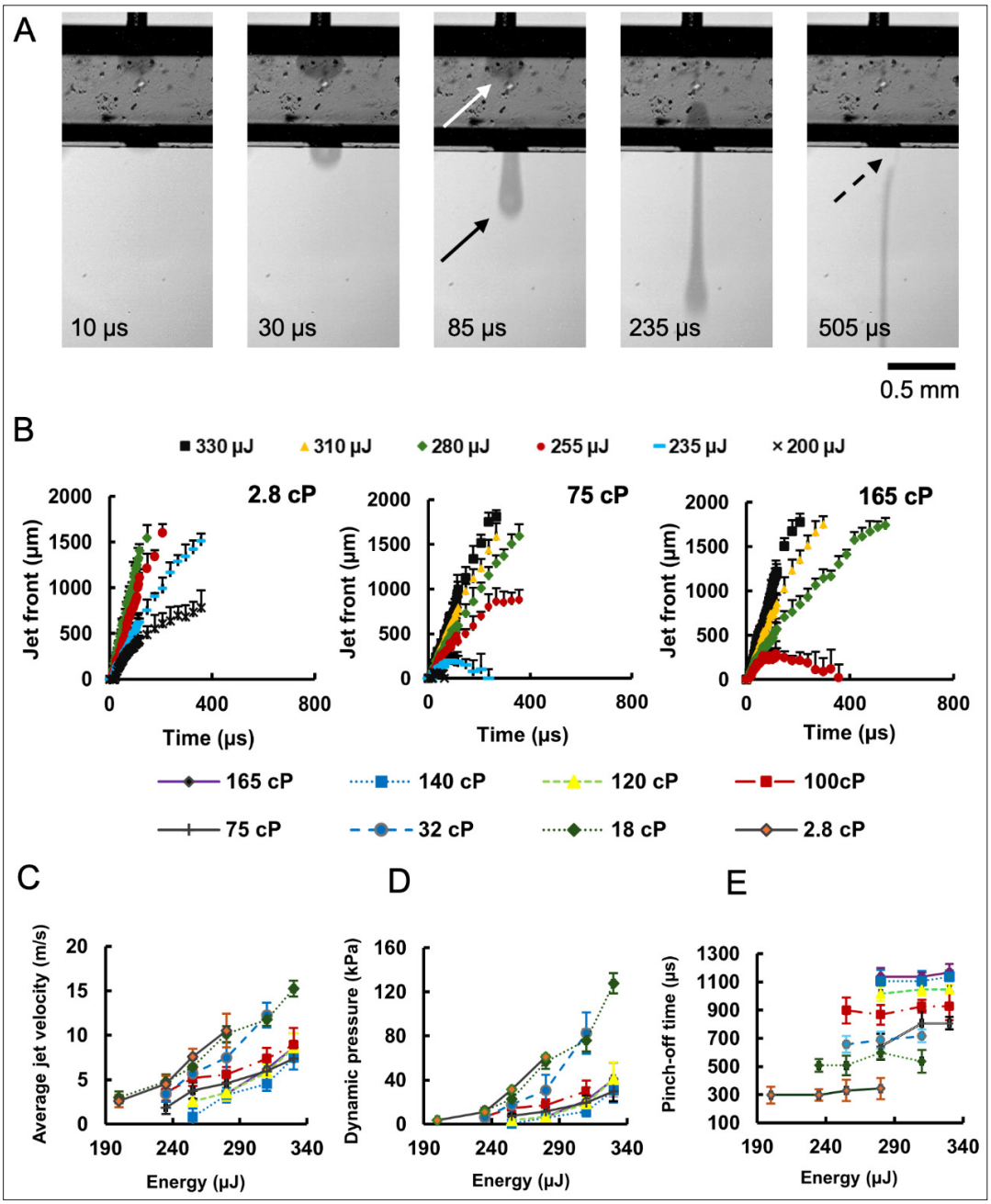

Figure 4. The effect of ink viscosity and laser energy on jetting dynamics. (A) A sequence of images taken with a high-speed camera showing the ejection of a microjet from the glass capillary opening. The solid white arrow indicates the bubble front, the solid black arrow indicates the jet front, and the dashed black arrow indicates the jet pinch-off. (B) The jet front position evolution for three viscosities (2.8 cP—left; 75 cP—middle; 165 cP—right). The dependence of (C) the average jet velocity, (D) dynamic pressure, and (E) pinch-off time on the laser pulse energy for different ink viscosities. Error bars represent the standard deviation from three independent printing experiments.

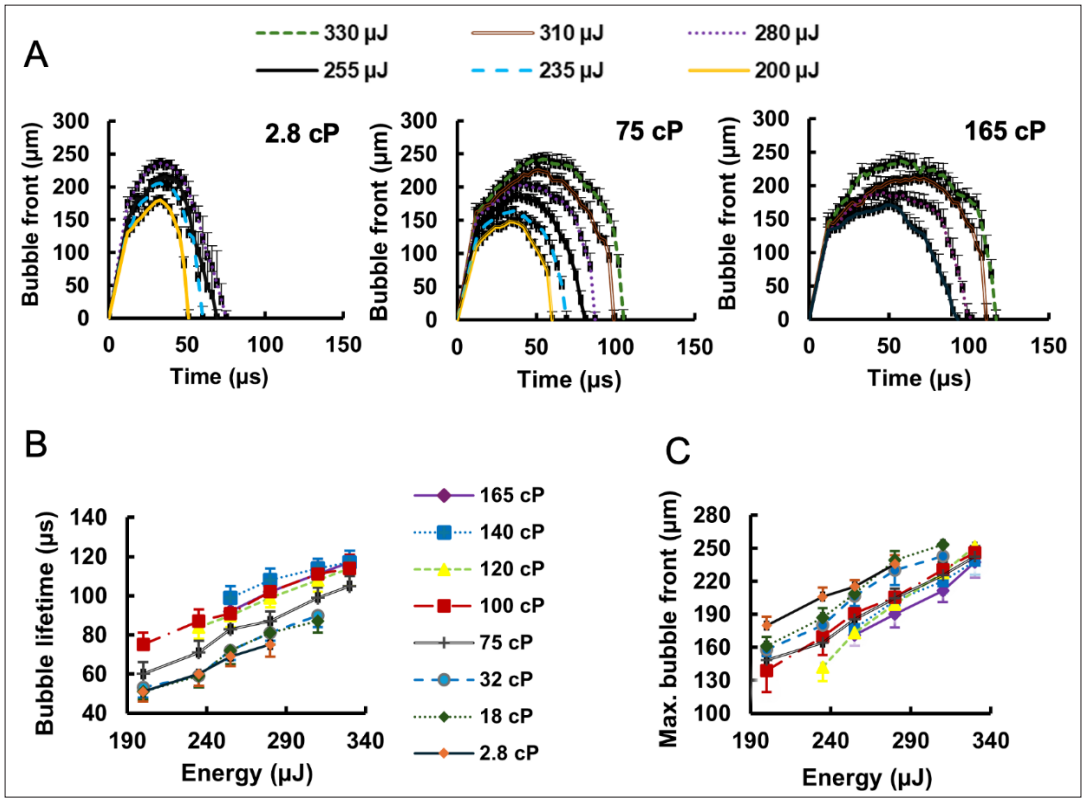

Figure 5. The effect of ink viscosity and laser energy on bubble dynamics. (A) The bubble front evolution for three viscosities (2.8 cP—left; 75 cP—middle; 165 cP—right). The dependence of (B) the bubble lifetime and (C) the maximum bubble front on the laser pulse energy for different ink viscosities. Error bars represent the standard deviation from three independent printing experiments.

to range from 297 ± 60 to 1167 ± 60 μs for the examined conditions, with pinch-off time increasing as viscosity increased for a given laser energy (Figure 4E).

Figure 5A shows the bubble evolution over time for three selected viscosities (2.8, 75, and 165), while the corresponding plots for all tested viscosities can be found in Figure S3, Supplementary File. The bubble lifetime varied from 51 ± 5 to 117 ± 6 μs for the examined conditions (Figure 5B), while the maximum bubble front ranged from 142.13 ± 5.71 to 261.54 ± 14.25 μm (Figure 5C). A clear trend in these graphs is that bubble lifetime increases with the viscosity, whereas the maximum bubble front decreases with increasing viscosity.

Using the images captured by the fast camera (Figure 4A), we calculated the bubble volume and jet volume under the examined conditions. The jet volume

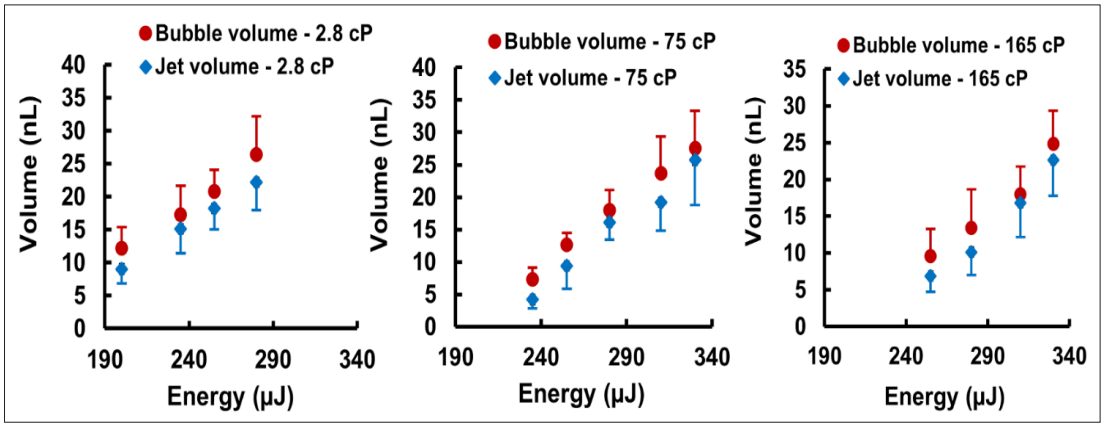

Figure 6. The dependence of the bubble and jet volume on the laser energy for three viscosities (2.8 cP—left; 75 cP—middle; 165 cP—right). Error bars represent the standard deviation from three independent printing experiments.

ranged from 4.17 ± 1.33 to 25.7 ± 6.9 nL and was consistently lower than the bubble volume, which ranged from 7.26 ± 1.83 to 27.56 ± 5.79 nL (Figure 6). Despite this difference, the jet and bubble volumes showed a consistent correlation across the different energies and viscosities.

Taken together, these results highlight the influence of ink viscosity on microjet ejection and bubble dynamics. Higher viscosities require more energy for jet ejection and slow down bubble dynamics, microjet formation, and the detachment process.

4. Discussion

This study aimed to develop and validate a mobile LIST printing platform, with a focus on investigating critical parameters that influence print quality, including head-to-substrate distance, ink viscosity, and motion compensation. Here we discuss the key findings in relation to current limitations and future directions in laser-based DoD printing.

Shape fidelity is crucial in bioprinting because it determines how closely a printed structure matches its intended design. In DoD printing, maintaining high fidelity in printed structures requires precise placement of each droplet on the substrate with minimal deviation or splashing. In this work a printing head-to-target distance of 3 mm was the upper limit for ensuring splatter-free printing. Distances greater than 3 mm resulted in a significant increase in splatter coverage, which reached 37.36 ± 13.01% at 24 mm. This increase can be attributed to the longer flight distance of the droplet, which increases its exposure to aerodynamic forces, causing potential disruptions in its shape or trajectory.[39] These disturbances may lead to droplet breakup into smaller droplets or scattering upon impact. To mitigate this, increasing the droplet ejection speed can reduce flight time and make the process less sensitive to variations in printing head-to-substrate distance, thereby improving positional accuracy.[40] However, caution is needed when increasing jet speed to avoid splashing upon substrate impact or unintended jet penetration, particularly if the target is soft.

Our OCT-based distance sensing approach proved effective in eliminating print quality loss when printing on a moving target, simulating physiological movements. This finding is particularly relevant for *in vivo* bioprinting applications, where the targeted anatomical defect may shift due to breathing, heartbeat, or unpredictable patient motion.[17,41] Previously developed automation systems for compensating target motion in 3D bioprinting are primarily machine vision-based[14,41] and are relatively bulky compared to the miniaturized fiber-based system (0.25 mm in diameter) developed in this work. These existing systems typically offer millimeter-scale precision in position tracking, whereas the OCT system presented here achieves micrometer-level precision. Therefore, this system is well suited for integration with extrusion-based bioprinters, where the required precision in maintaining the nozzle-to-target distance is an order of magnitude higher than in DoD systems.

The central mechanism in the LIST printing process is nanosecond laser-induced thermocavitation—a rapid, localized phenomenon initiated by the interaction of nanosecond laser pulses with highly-absorbing liquid.[42,43] Nanosecond laser pulses rapidly heat a small volume of liquid, leading to near-instantaneous vaporization and bubble formation. The bubble expands until its internal pressure equilibrates with ambient pressure at its maximum radius, after which it collapses due to compression by the surrounding liquid. The growth and collapse dynamics of these bubbles are influenced by the physical properties of the liquid medium, particularly its viscosity. In this work, we found that higher ink viscosities slow down bubble dynamics. This is a consistent with the fact that in viscous fluids, internal friction resists flow, resulting in slower fluid motion.[44] When the same amount of energy (e.g., from a laser pulse) is applied, a greater proportion is dissipated through viscous forces, leaving less energy available for bubble expansion. Consequently, bubble growth in high-viscosity inks is slower and reaches a smaller maximum radius compared to low-viscosity fluids.[45,46] We also found that higher viscosities require greater energy for jet ejection and lead to longer jet pinch-off times. This is primarily because viscous fluids resist necking flow, allowing the liquid column to sustain elongation for a longer duration before breaking. This behavior is observed in both inkjet and laser-assisted bioprinting. For instance, in alginate inkjet printing, increasing the sodium alginate (NaAlg) concentration from 0.15% to 2% (w/v)—and thus increasing viscosity—results in a fourfold increase in droplet pinch-off time.[47]

The Ohnesorge number (Oh) is a key dimensionless parameter used to evaluate the jetting behavior of fluids. It encapsulates the balance between viscous, inertial, and surface tension forces, and is defined as $Oh = \mu/\sqrt{(\rho\sigma d)}$, where μ is the dynamic viscosity, ρ the fluid density, σ the surface tension, and d the characteristic length scale (typically the nozzle or jet diameter).[48] In this work, the Ohnesorge number ranged from 0.021 for the lowest-viscosity ink (2.8 cP) to 1.31 for the highest-viscosity ink (165 cP). In accordance with our results, Newtonian fluids in the Ohnesorge number range of 0.01 to ~1.5 have been shown to produce stable, satellite-free droplets in laser-assisted flow-focusing systems.[25] The Weber number (We) was also calculated to characterize the ratio of inertial to

surface tension forces, defined as We = $(\rho v^2 d)/\sigma$, where v is the jet velocity. The Weber number is useful for assessing droplet behavior upon impact, such as splashing or penetration into soft substrates (e.g., tissue).[49,50] Across all tested viscosities and laser energies using the mobile LIST printer, the Weber number ranged from 20 to 320—placing it well within the drop spreading regime and avoiding conditions associated with splashing or substrate penetration when targeting soft tissue.[51]

Compared to our previous LIST implementation using a fixed printing head with free-space optics,[28] the present mobile fiber-based setup shows a consistently higher printing threshold energy—by a factor of 1.5—across all tested viscosities (2.8–140 cP) with the same model ink. Two factors likely contribute to this difference. The primary factor is that, in the mobile fiber-based setup, the bubble is generated at the top part of the capillary, which is farther from the opening compared to the free-space optics system, where the bubble forms in the middle of the capillary. The second factor is the focusing lens used in the fixed setup, which produced a smaller spot size compared to the 105 μm fiber output, thereby yielding a higher power density at the focus for the same deposited energy. Nevertheless, both systems achieved printing over a similar viscosity range.

One limitation of the present study is that printing experiments were conducted using a step-by-step movement of the robotic arm rather than continuous motion along predefined paths. This was necessary due to the need for continuous Z-coordinate updates using input from the OCT-based position tracking system. However, this operational mode introduced vibrations, which significantly contributed to drop placement errors. For instance, when the update frequency of the XYZ coordinates was reduced from 5 to 2 Hz, the droplet placement error decreased from 220 ± 113 to 119 ± 57 μm at 3 mm. This suggests that mechanical instability and vibrations in the robotic arm play an important role in accuracy limitations. This issue could potentially be mitigated by using a robotic arm that is less susceptible to vibration, or by employing a separate end-effector dedicated to Z-positioning, thus decoupling vertical adjustments from general motion.

In experiments conducted without Z-position adjustment, the mobile LIST printer operated smoothly at frequencies up to 30 Hz, which corresponds to the maximum repetition rate of our current laser system. Based on the observed pinch-off times, frequencies as high as 800 Hz appear to be theoretically feasible, although this has yet to be experimentally confirmed.

We employed an FDA-approved dye to enhance the model ink's absorption coefficient at 532 nm. While effective for energy absorption, this dye imparts a red coloration to the printed constructs. The dye does not pose biocompatibility concerns,[26–28,34,35] but the coloration may not be entirely washable from some matrices. This may limit the use of this approach in applications that require high optical transparency. One potential solution is to shift to mid-infrared laser sources, where water exhibits a much higher absorption coefficient.[52,53] These wavelengths have already been successfully applied in donor-free LIFT bioprinting,[54,55] suggesting a promising path forward for dye-free LIST.

5. Conclusion

In conclusion, we successfully developed and validated a mobile, laser-assisted DoD printing head integrated with a robotic arm and an optical distance sensor. Printing volumes for model inks with viscosities up to 165 cP were in the nanoliter range. Higher viscosities required increased laser energy and resulted in longer jet pinch-off times. Our results highlight that maintaining a printing head-to-target distance below 3 mm is essential for preserving print quality, and that our dynamic distance compensation effectively mitigates printing quality loss on targets simulating physiological motion. This compact, mobile DoD system can facilitate *in situ* bioprinting applications in dynamic physiological environments.

Acknowledgments

The authors thank Jennyfer Zapata-Farfan and the Meunier lab at Polytechnique Montreal for machining the glass capillaries used in this work. Ahad Mohammadi is a recipient of a PhD scholarship funded by the Hôpital Maisonneuve-Rosemont Foundation. Shakiba Davani is a recipient of a PhD scholarship from the Fonds de recherche en ophtalmologie de l'Université de Montréal.

Funding

Christos Boutopoulos acknowledges financial support from the Canadian Institutes of Health Research (#527176), the Natural Sciences and Engineering Research Council (NSERC) (#RGPIN-2025-07077), the Fonds de la recherche en santé du Québec (FRQS) (#312263), and the Canada Foundation for Innovation (#43112).

Conflict of interest

The authors declare they have no competing interests.

Author contributions

Conceptualization: Ahad Mohammadi, Christos Boutopoulos
Formal analysis: Ahad Mohammadi
Funding acquisition: Christos Boutopoulos

Investigation: Ahad Mohammadi, Shakiba Davani, Christos Boutopoulos
Methodology: Ahad Mohammadi, Shakiba Davani, Christos Boutopoulos
Supervision: Christos Boutopoulos
Visualization: Ahad Mohammadi, Christos Boutopoulos
Writing–original draft: Ahad Mohammadi
Writing–review & editing: Ahad Mohammadi, Shakiba Davani, Christos Boutopoulos

Ethics approval and consent to participate

Not applicable.

Consent for publication

Not applicable.

Availability of data

The data can be obtained from the corresponding author upon reasonable request.

References

1. Leberfinger AN, Dinda S, Wu Y, *et al.* Bioprinting functional tissues. *Acta Biomater.* 2019;95:32-49. doi: 10.1016/j.actbio.2019.01.009.
2. Xu H-Q, Liu J-C, Zhang Z-Y, Xu C-X. A review on cell damage, viability, and functionality during 3D bioprinting. *Mil Med Res.* 2022;9(1):70-82. doi: 10.1186/s40779-022-00429-5.
3. Abuwatfa WH, Pitt WG, Husseini GA. Scaffold-based 3D cell culture models in cancer research. *J Biomed Sci.* 2024;31(1):7-20. doi: 10.1186/s12929-024-00994-y.
4. Lam EHY, Yu F, Zhu S, Wang Z. 3D bioprinting for next-generation personalized medicine. *Int J Mol Sci.* 2023;24(7):6357-6379. doi: 10.3390/ijms24076357.
5. Pathak K, Saikia R, Das A, *et al.* 3D printing in biomedicine: advancing personalized care through additive manufacturing. *Explor Med.* 2023;4(6):1135-1167. doi: 10.37349/emed.2023.00200.
6. Kim M, Kim YJ, Kim YS, *et al.* One-year results of ear reconstruction with 3D printed implants. *Yonsei Med J.* 2024;65(8):456-463. doi: 10.3349/ymj.2023.0444.
7. Singh S, Choudhury D, Yu F, Mironov V, Naing MW. In situ bioprinting—bioprinting from benchside to bedside? *Acta Biomater.* 2020;101:14-25. doi: 10.1016/j.actbio.2019.08.045.
8. MacAdam A, Chaudry E, McTiernan CD, *et al.* Development of in situ bioprinting: a mini review. *Front Bioeng Biotechnol.* 2022;10:940896. doi: 10.3389/fbioe.2022.940896.
9. Li H, Cheng F, Orgill DP, Yao J, Zhang YS. Handheld bioprinting strategies for in situ wound dressing. *Essays Biochem.* 2021;65(3):533-543. doi: 10.1042/EBC20200098.
10. Jain P, Kathuria H, Ramakrishna S, *et al.* In situ bioprinting: process, bioinks, and applications. *ACS Appl Bio Mater.* 2024;7(12):7987-8007. doi: 10.1021/acsabm.3c01303.
11. Kérourédan O, Hakobyan D, Rémy M, *et al.* In situ prevascularization designed by laser-assisted bioprinting: effect on bone regeneration. *Biofabrication.* 2019;11(4):045002. doi: 10.1088/1758-5090/ab2620.
12. Keriquel V, Oliveira H, Rémy M, *et al.* In situ printing of mesenchymal stromal cells by laser-assisted bioprinting for in vivo bone regeneration applications. *Sci Rep.* 2017;7(1):1778-1788. doi: 10.1038/s41598-017-01914-x.
13. Pazhouhnia Z, Beheshtizadeh N, Namini MS, *et al.* Portable hand-held bioprinters promote in situ tissue regeneration. *Bioeng Transl Med.* 2022;7(3):e10307. doi: 10.1002/btm2.10307.
14. Fortunato GM, Bonatti AF, Batoni E, *et al.* Motion compensation system for robotic based in situ bioprinting to balance patient physiological movements. *Bioprinting.* 2022;28:e00248. doi: 10.1016/j.bprint.2022.e00248.
15. Zhao W, Hu C, Xu T. In vivo bioprinting: broadening the therapeutic horizon for tissue injuries. *Bioact Mater.* 2023;25:201-222. doi: 10.1016/j.bioactmat.2023.01.018.
16. Samandari M, Mostafavi A, Quint J, *et al.* In situ bioprinting: intraoperative implementation of regenerative medicine. *Trends Biotechnol.* 2022;40(10):1229-1247. doi: 10.1016/j.tibtech.2022.03.009.
17. Li K, Huang W, Guo H, *et al.* Advancements in robotic arm-based 3D bioprinting for biomedical applications. *Life Med.* 2023;2(6):lnad046. doi: 10.1093/lifemedi/lnad046.
18. Yang Y, Cai Y, Jung Yoon Y, Zhao H, Gupta SK. Sensor-based planning and control for conformal deposition on a deformable surface using an articulated industrial robot. *J Manuf Sci Eng.* 2024;146(1):011005. doi: 10.1115/1.4063560.
19. Li X, Liu B, Pei B, *et al.* Inkjet bioprinting of biomaterials. *Chem Rev.* 2020;120(19):10793-10833. doi: 10.1021/acs.chemrev.0c00008.

20. Serra P, Piqué A. Laser-induced forward transfer: fundamentals and applications. *Adv Mater Technol.* 2019;4(1):1800099. doi: 10.1002/admt.201800099.

21. Morales M, Munoz-Martin D, Marquez A, *et al.* Laser-induced forward transfer techniques and applications. *Adv Laser Mater Process.* 2018:339-379. doi: 10.1016/B978-0-08-101252-9.00013-3.

22. Fernández-Pradas J, Colina M, Serra P, *et al.* Laser-induced forward transfer of biomolecules. *Thin Solid Films.* 2004;453(1-2):27-30. doi: 10.1016/j.tsf.2003.11.154.

23. Elezoglou S, Hatziapostolou A, Giannakopoulos K, *et al.* High-precision depth-controlled laser bioprinting of cells in extracellular matrix for three-dimensional structures. *Int J Bioprint.* 2025;11(3):292-306. doi: 10.36922/IJB025100082.

24. Koch L, Deiwick A, Soriano J, *et al.* Laser bioprinting of human iPSC-derived neural stem cells and neurons: effect on cell survival, multipotency, differentiation, and neuronal activity. *Int J Bioprint.* 2023;9(2):672-684. doi: 10.18063/ijb.v9i2.672.

25. Delrot P, Modestino MA, Gallaire F, *et al.* Inkjet printing of viscous monodisperse microdroplets by laser-induced flow focusing. *Phys Rev Appl.* 2016;6(2):024003. doi: 10.1103/PhysRevApplied.6.024003.

26. Ebrahimi Orimi H, Hosseini Kolkooh SS, Hooker E, *et al.* Drop-on-demand cell bioprinting via laser induced side transfer (LIST). *Sci Rep.* 2020;10(1):9730-9740. doi: 10.1038/s41598-020-66565-x.

27. Roversi K, Ebrahimi Orimi H, Falchetti M, *et al.* Bioprinting of adult dorsal root ganglion (DRG) neurons using laser-induced side transfer (LIST). *Micromachines.* 2021;12(8):865-875. doi: 10.3390/mi12080865.

28. Erfanian M, Mohammadi A, Orimi HE, *et al.* Drop-on-demand bioprinting: a redesigned laser-induced side transfer approach with continuous capillary perfusion. *Int J Bioprint.* 2024;10(3):2832-2845. doi: 10.36922/ijb.2832.

29. Sheely ML. Glycerol viscosity tables. *Ind Eng Chem.* 1932;24(9):1060-1064. doi: 10.1021/ie50273a022.

30. Pope RM, Fry ES. Absorption spectrum (380–700 nm) of pure water. II. Integrating cavity measurements. *Appl Opt.* 1997;36(33):8710-8723. doi: 10.1364/AO.36.008710.

31. Reddy RS, Alahmari KA, Silvian PS, *et al.* Reliability of chest wall mobility and its correlation with lung functions in healthy nonsmokers, healthy smokers, and patients with COPD. *Can Respir J.* 2019;2019:5175949. doi: 10.1155/2019/5175949.

32. Abid A, Duval R, Rezende F, *et al.* A smart vitrector equipped by a fiber-based OCT sensor mitigates intentional attempts at creating iatrogenic retinal breaks during vitrectomy in pigs. *Transl Vis Sci Technol.* 2021;10(13):19. doi: 10.1167/tvst.10.13.19.

33. Abid A, Mittal S, Boutopoulos C. Etching-enabled extreme miniaturization of graded-index fiber-based optical coherence tomography probes. *J Biomed Opt.* 2020;25(3):032006. doi: 10.1117/1.JBO.25.3.032006.

34. Roversi K, Orimi HE, Erfanian M, *et al.* LIST: a newly developed laser-assisted cell bioprinting technology. *Bio Protoc.* 2022;12(19):e4527. doi: 10.21769/BioProtoc.4527.

35. Orimi HE, Hooker E, Narayanswamy S, *et al.* Spatially guided endothelial tubulogenesis by laser-induced side transfer (LIST) bioprinting of HUVECs. *Bioprinting.* 2022;28:e00240. doi: 10.1016/j.bprint.2022.e00240.

36. Thalheim R, Willert A, Mitra D, *et al.* Novel and efficient methodology for drop placement accuracy testing of robot-guided inkjet printing onto 3D objects. *Machines.* 2023;11(5):568-579. doi: 10.3390/machines11050568.

37. Antonopoulou E, Harlen O, Walkley M, *et al.* Jetting behavior in drop-on-demand printing: laboratory experiments and numerical simulations. *Phys Rev Fluids.* 2020;5(4):043603. doi: 10.1103/PhysRevFluids.5.043603.

38. Krainer S, Smit C, Hirn U. The effect of viscosity and surface tension on inkjet printed picoliter dots. *RSC Adv.* 2019;9(54):31708-31719. doi: 10.1039/C9RA04993B.

39. Cimpeanu R, Papageorgiou DT. Three-dimensional high speed drop impact onto solid surfaces at arbitrary angles. *Int J Multiph Flow.* 2018;107:192-207. doi: 10.1016/j.ijmultiphaseflow.2018.06.011.

40. Wijshoff H. The dynamics of the piezo inkjet printhead operation. *Phys Rep.* 2010;491(4-5):77-177. doi: 10.1016/j.physrep.2010.03.003.

41. Zhu Z, Guo SZ, Hirdler T, *et al.* 3D printed functional and biological materials on moving freeform surfaces. *Adv Mater.* 2018;30(23):1707495. doi: 10.1002/adma.201707495.

42. Zaca-Morán R, Amaxal-Cuatetl C, Zaca-Moran P, *et al.* Thermocavitation: a mechanism to pulse fiber lasers. *Opt Express.* 2021;29(15):23439-23446. doi: 10.1364/OE.430319.

43. Schoppink JJ, Alvarez-Chavez JA, Fernandez Rivas D. Laser beam properties and microfluidic confinement control thermocavitation. *Appl Phys Lett.* 2024;124(1):011101. doi: 10.1063/5.0186998.

44. Derby B. Inkjet printing of functional and structural materials: fluid property requirements, feature stability, and resolution. *Annu Rev Mater Res.* 2010;40(1):395-414. doi: 10.1146/annurev-matsci-070909-104502.

45. Chang J, Sun X. Laser-induced forward transfer based laser bioprinting in biomedical applications. *Front Bioeng Biotechnol.* 2023;11:1255782. doi: 10.3389/fbioe.2023.1255782.

46. Wang X, Ning Z, Lv M, *et al.* Machine learning for predicting the bubble-collapse strength as affected by physical conditions. *Results Phys.* 2021;25:104226. doi: 10.1016/j.rinp.2021.104226.

47. Xu C, Zhang M, Huang Y, *et al.* Study of droplet formation process during drop-on-demand inkjetting of living cell-laden bioink. *Langmuir.* 2014;30(30):9130-9138. doi: 10.1021/la501430x.

48. Tai J, Gan HY, Liang YN, *et al.* Control of droplet formation in inkjet printing using Ohnesorge number. *Proc Electron Packag Technol Conf.* 2008:761-766. doi: 10.1109/EPTC.2008.4763524.

49. Qian S, Zhu DZ, Xu H. Splashing generation by water jet impinging on a horizontal plate. *Exp Therm Fluid Sci.* 2022;130:110518. doi: 10.1016/j.expthermflusci.2021.110518.

50. Yarin AL. Drop impact dynamics: splashing, spreading, receding, bouncing. *Annu Rev Fluid Mech.* 2006;38:159-192. doi: 10.1146/annurev.fluid.38.050304.092144.

51. van der Ven DL, Morrone D, Quetzeri-Santiago MA, *et al.* Microfluidic jet impact: spreading, splashing, soft substrate deformation and injection. *J Colloid Interface Sci.* 2023;636:549-558. doi: 10.1016/j.jcis.2023.01.024.

52. Jang HJ, Yu H, Lee S, *et al.* Towards clinical use of a laser-induced microjet system aimed at reliable and safe drug delivery. *J Biomed Opt.* 2014;19(5):058001. doi: 10.1117/1.JBO.19.5.058001.

53. Ishikawa I, Aoki A, Takasaki AA. Potential applications of Erbium:YAG laser in periodontics. *J Periodont Res.* 2004;39(4):275-285. doi: 10.1111/j.1600-0765.2004.00738.x.

54. Cheptsov V, Minaev N, Zhigarkov V, *et al.* Laser bioprinting without donor plate. *Laser Phys Lett.* 2022;19(8):085602. doi: 10.1088/1612-202X/ac7b32.

55. Pushkin AV, Minaev NV, Potemkin FV, *et al.* Bioprinting with 3-μm laser pulses. *Opt Laser Technol.* 2024;172:110482. doi: 10.1016/j.optlastec.2023.110482.